

KINETICS, CATALYSIS, AND REACTION ENGINEERING

Hot Zones Formation and Dynamics in Long Adiabatic Packed-Bed Reactors

Ganesh A. Viswanathan[†] and Dan Luss*

Department of Chemical Engineering, University of Houston, Houston, Texas 77204-4004

Transversal (normal to the flow direction) hot zones have been reported to form in packed-bed reactors. While hot zones may form due to local nonuniformities in the local activity or porosity, they may form also in a strictly uniform reactor for certain classes of reaction kinetics. For example, they are predicted to form in an adiabatic packed-bed reactor using realistic parameters when the catalytic reaction rate oscillates under some constant ambient conditions. Qualitatively different hot zones may form in the bed for the same set of parameters. A systematic procedure is outlined to predict the set of parameters for which such spatiotemporal temperature patterns may form. Dynamic simulations of a 2-D long packed-bed reactor model (one that ignores the azimuthal dependence) reveal the existence of complex periodic motions (period-2, -4, -8) as well as chaos. The transversal features of these periodic motions resemble those of several transversal modes predicted by the linear stability analysis. Spatial snapshots of the chaotic motion strongly suggest that it was caused by modulation and juxtaposition among motions corresponding to different modes.

Introduction

The formation of local transversal (normal to the flow direction) hot zones in adiabatic packed-bed reactors may decrease the yield of the product, deactivate the catalyst, or initiate undesired highly exothermic reactions, leading to a potential runaway. The presence of hot zones next to the reactor wall may decrease its strength and induce a crack. The subsequent leak of the reactants can lead to an explosion. Several trickle-bed reactor explosions have been attributed to the presence of such local hot zones. Hot zones have been observed in both industrial and laboratory packed-bed reactors. Boreskov et al.¹ and Matros² observed several azimuthally nonsymmetric hot zones at the cross section of the top of a packed-bed reactor in which the partial oxidation of isobutyl alcohol was conducted using a copper catalyst. Barkelew and Gambhir³ reported clinker formation—small lumps of molten catalyst—during hydrodesulfurization in trickle-bed reactors. Jaffe⁴ reported hot-spot formation during a hydrogenation reaction. Wicke and Onken^{5,6} observed a transversal temperature nonuniformity in a laboratory packed-bed reactor during the oxidation of CO. Intricate spatiotemporal, transversal temperature patterns were observed using infrared imaging on top of a shallow packed-bed reactor^{7,8} and on the external surface of a radial-flow reactor.^{9,10} Qualitatively similar complex hot-zone motions were observed by Digilov et al.¹¹ on a catalytic glass fiber cloth reactor and by Digilov et al.¹² on the surface of a thin annular catalytic shell. Sundarram et al.¹³ pointed out that global coupling between the effluents and the top of the reactor affected these temperature patterns.

Local hot spots may form in packed-bed reactors due to the nonuniformity of the catalyst activity or of the packing of the

bed, as reported by Matros.² Other potential causes can be local obstruction of the flow,⁴ hydrodynamic instabilities,^{14,15} or global coupling caused by interaction between the top of the reactor and the mixed effluents^{13,16} or between the reactants and the surface of a thin cylindrical catalytic reactor.^{12,17}

There have been several related attempts to predict formation of hot zones in a uniform packed-bed reactor, that is, one in which the porosity and activity are the same throughout the whole bed. Schmitz and Tsotsis¹⁸ predicted that stationary temperature patterns may form in a chain of interacting catalyst pellets when the species exchange exceeded that of heat. Balakotaiah et al.¹⁹ showed that temperature patterns may form in an adiabatic packed-bed reactor used to conduct an exothermic bimolecular reaction with Langmuir–Hinshelwood kinetics, if the rate of the transversal species dispersion exceeds that of the heat dispersion. However, Yakhnin and Menzinger²⁰ pointed out that in packed-bed reactors the dispersion of heat is larger than that of the species. Sheintuch's group has shown that stable 2-D hot regions may form on the external surface of a thin cylindrical catalytic shell when the reactants flow along its surface, using a model that accounted also for global interaction.^{12,17} These nonuniform azimuthal surface temperatures are different from the 3-D hot zones that exist at different radial and azimuthal positions in a cross section of a packed bed and are not influenced by global coupling.

We recently initiated a study in which models of an adiabatic packed-bed reactor can predict the formation of a stable temperature pattern. We were able to prove^{21,22} that, when the reaction rate depends only on the surface concentration of the limiting reactant and temperature, common models of a shallow adiabatic packed-bed reactor cannot predict bifurcation to a stable, stationary temperature pattern, if they account for the fact that the transversal dispersion of heat exceeds that of the reactants. We then showed that the formation of stable hot zones in a uniform, shallow adiabatic packed-bed reactor is sensitive

* To whom inquiries should be addressed. E-mail: Dluss@uh.edu.

[†] Present address: Department of Neurology, Mount Sinai School of Medicine, One Gustave L. Levy Place, Box 1137, New York, NY 10029.

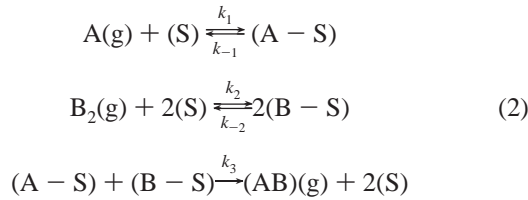
to the kinetics of the reactions.²³ For example, spatiotemporal temperature patterns may form in a shallow adiabatic packed-bed reactor using realistic parameters when the rate of the catalytic reaction oscillates under constant ambient conditions. Various tested rate expressions, such as those describing CO oxidation, exhibit this feature. Asakura et al.²⁴ described reaction mechanisms that can lead to isothermal concentration oscillations on catalytic surfaces. We extend here the investigation of hot-zone formation and dynamics in a shallow packed bed to the more realistic case of a long adiabatic packed-bed reactor.

Mathematical Model

We consider an adiabatic packed-bed reactor in which the following reaction takes place:



We assume that the reaction proceeds by a Langmuir–Hinshelwood mechanism



Species A and species B—which is in large excess in the feed—adsorb on the active free sites S. We assume that the product (AB) immediately desorbs from the catalyst surface soon after it forms. Following Slinko and co-workers,^{25–27} we assume that the reaction rate constant k_3 depends on the fractional surface coverage of species B, y_B . This reaction exhibits isothermal oscillations for some kinetic parameters. A kinetic model²⁷ of this reaction, which includes a minimal number of parameters, is

$$\frac{dy_A}{d\tau} = G_1(y_A, y_B, x, \theta) - R(y_A, y_B, \theta) \quad (3)$$

$$\frac{dy_B}{d\tau} = G_2(y_A, y_B, \theta) - R(y_A, y_B, \theta) \quad (4)$$

where y_A is the surface coverage of species A, x is the conversion of species A, and θ is the dimensionless temperature. The expressions describing G_1 , the net rate of adsorption of A; G_2 , the net rate of adsorption of B; and R , the reaction rate per unit surface area of the catalyst, are as follows:

$$\begin{aligned} G_1(y_A, y_B, x, \theta) &= Da_1 \exp\left(\frac{\gamma_1 \theta}{1 + \theta}\right) (1 - x)(1 - y_A - y_B) - \\ &Da_{-1} \exp\left(\frac{\gamma_{-1} \theta}{1 + \theta}\right) y_A \end{aligned} \quad (5)$$

$$\begin{aligned} G_2(y_A, y_B, \theta) &= Da_2 \exp\left(\frac{\gamma_2 \theta}{1 + \theta}\right) (1 - y_A - y_B)^2 - \\ &Da_{-2} \exp\left(\frac{\gamma_{-2} \theta}{1 + \theta}\right) y_B^2 \end{aligned} \quad (6)$$

$$R(y_A, y_B, \theta) = Da \exp\left(\frac{\gamma_3 \theta}{1 + \theta}\right) y_A y_B \exp(-\mu y_B) \quad (7)$$

where μ is the fractional surface coverage factor. The dimensionless variables and parameters are

$$x = (C_{A,\text{in}} - C_A)/C_{A,\text{in}}, \quad \theta = (T - T_{\text{in}})/T_{\text{in}}$$

$$\tau = tv/L$$

$$\begin{aligned} Da_1 &= \frac{k_1(T_{\text{in}})C_{A,\text{in}}L}{\nu}, \quad Da_{-1} = \frac{k_{-1}(T_{\text{in}})L}{\nu} \\ Da_2 &= \frac{2k_2(T_{\text{in}})C_{B,\text{in}}L}{\nu}, \quad Da_{-2} = \frac{2k_{-2}(T_{\text{in}})L}{\nu} \end{aligned} \quad (8)$$

$$Da = \frac{k_3(T_{\text{in}})L}{\nu}, \quad \gamma_i = E_i/(\bar{R}T_{\text{in}})$$

$$k_i(T_{\text{in}}) = k_{i0} \exp(-\gamma_i) \quad \forall i = 1, -1, 2, -2, 3$$

$C_{A,\text{in}}$, $C_{B,\text{in}}$, and T_{in} are the feed concentrations of species A and B and the feed temperature, respectively. A detailed discussion of this class of kinetic models that assumes a simple Langmuir–Hinshelwood mechanism and a slow variation in the catalytic activity are discussed in detail in the monograph by Slinko and Jaeger.²⁸ The kinetic parameters of this type of model that describe the oscillatory rate of CO oxidation have been reported by Slinko et al.²⁹

We describe the reactor by a pseudo-homogeneous model that accounts for the adsorption of the reactants from the fluid phase to the catalyst sites, and in which the heat dispersion is larger than that of the species. We assume that the physical properties are independent of the temperature and species concentration. The conversion of the gaseous reactant A and the dimensionless temperature satisfy the equations

$$\frac{\partial x}{\partial \tau} = \frac{1}{Pe_{\perp}^m} \nabla_{\perp}^2 x + \frac{1}{Pe_a^m} \frac{\partial^2 x}{\partial \eta^2} - \frac{\partial x}{\partial \eta} + N_c G_1(y_A, y_B, x, \theta) \quad (9)$$

$$\frac{\partial \theta}{\partial \tau} = \frac{1}{Le} \left[\frac{1}{Pe_{\perp}^h} \nabla_{\perp}^2 \theta + \frac{1}{Pe_a^h} \frac{\partial^2 \theta}{\partial \eta^2} - \frac{\partial \theta}{\partial \eta} + \beta N_c R(y_A, y_B, \theta) \right] \quad (10)$$

where ∇_{\perp}^2 is the Laplacian in polar (ξ, ϕ) coordinates. The dimensionless variables and parameters are

$$\begin{aligned} \eta &= z/L, \quad \xi = r/R, \quad N_c = a_v M / C_{A,\text{in}} \\ Pe_a^h &= \frac{\nu L}{\bar{\lambda}_a / (\rho C_p)_g}, \quad Pe_a^m = \nu L / D_a, \quad \beta = \frac{(-\Delta H) C_{A,\text{in}}}{(\rho C_p)_g T_{\text{in}}} \\ Pe_{\perp}^h &= \frac{\nu R^2}{L \bar{\lambda}_{\perp} / (\rho C_p)_g}, \quad Pe_{\perp}^m = \nu R^2 / (LD_{\perp}), \\ Le &= \epsilon + (1 - \epsilon) \frac{(\rho C_p)_s}{(\rho C_p)_g} \end{aligned} \quad (11)$$

where M is the surface adsorption capacity, D is the species dispersion, and $\bar{\lambda}$ is the effective thermal dispersion. The transversal heat and species dispersion coefficients ($\bar{\lambda}_{\perp}$ and D_{\perp})

Table 1. First Nine Transverse Eigenmode Numbers Satisfying Eq 16

No.	<i>m</i>	<i>n</i>	μ_{mn}	No.	<i>m</i>	<i>n</i>	μ_{mn}
1	1	1	1.8412	6	1	2	5.3314
2	2	1	3.0542	7	5	1	6.4156
3	0	1	3.8317	8	2	2	6.7061
4	3	1	4.2012	9	0	2	7.0155
5	4	1	5.3176				

differ from those in the axial direction ($\bar{\lambda}_a$ and D_a). The corresponding boundary conditions are as follows:

$$\frac{1}{Pe_a^m} \frac{\partial x}{\partial \eta} = x \quad \frac{1}{Pe_a^h} \frac{\partial \theta}{\partial \eta} = \theta \quad \eta = 0 \quad (12)$$

$$\frac{\partial \theta}{\partial \eta} = \frac{\partial x}{\partial \eta} = 0 \quad \eta = 1 \quad (13)$$

$$\frac{\partial \theta}{\partial \xi} = \frac{\partial x}{\partial \xi} = 0 \quad \xi = 1 \quad (14)$$

Viswanathan and Luss²³ have shown that, for this reaction, spatiotemporal transversal temperature patterns may form in a shallow adiabatic packed-bed reactor. We obtained bounds on the range of parameters for which transversal hot zone may exist using linear stability analysis to determine when a stable, uniform state becomes unstable with respect to nonuniform perturbations.

Linear Stability Analysis

The procedure we used to determine the parameters at which a stable, uniform state of a long reactor becomes unstable to nonuniform perturbations is an extension of the one used to predict this stability shift in a shallow reactor.²³ The procedure is similar but more intricate as the 1-D base steady-state solution, which ignores the transversal dependence in a long reactor, $\mathbf{u}_{ss}(\eta) = (y_A, y_B, x, \theta)_{ss}$, is nonuniform. We briefly sketch the procedure here. A steady state is stable to homogeneous perturbations when all the eigenvalues of its Jacobian have a negative real part. At a limit point, a real eigenvalue crosses the imaginary axis. A Hopf bifurcation occurs when a pair of eigenvalues crosses the imaginary axis at a nonzero speed. At a supercritical Hopf bifurcation point, a stable (transversally uniform) periodic solution emerges from a stable, transversally uniform 1-D steady state.

At a neutral stability point, a 1-D base state becomes unstable to spatially inhomogeneous perturbations

$$\boldsymbol{\omega}_{mn}(\eta) = \boldsymbol{\omega}(\eta) J_m(\mu_{mn} \xi) e^{im\phi} \quad (15)$$

where *m* and *n* are the radial and azimuthal mode numbers. $e^{im\phi}$ and J_m , the Bessel function of the first kind, are the azimuthal and radial eigenfunctions (of the transversal operator), and $\boldsymbol{\omega}(\eta) = \boldsymbol{\omega}_r(\eta) \pm i\boldsymbol{\omega}_i(\eta)$ are the complex eigenvectors. Because of the no-flux boundary conditions, J_m is real³⁰ and μ_{mn} , the transversal eigenmode numbers, are the solutions of¹⁹

$$\left. \frac{dJ_m(\mu_{mn} \xi)}{d\xi} \right|_{\xi=1} = mJ_m(\mu_{mn}) - \mu_{mn} J_{m+1}(\mu_{mn}) = 0 \quad (16)$$

The first nine values of μ_{mn} are presented in Table 1, and a schematic of the corresponding first six modes is presented elsewhere.²¹

Linearization of the model equations (eqs 3, 4, 9, and 10) around the 1-D base state and subjecting it to the spatially

inhomogeneous perturbations (eq 15) leads to the following eigenvalue problem

$$\begin{aligned} & - \left[Da_1 \exp\left(\frac{\gamma_1 \theta}{1 + \theta}\right) (1 - x) + Da_{-1} \exp\left(\frac{\gamma_{-1} \theta}{1 + \theta}\right) + \right. \\ & \left. \frac{\partial \mathcal{R}}{\partial y_A} \right] \Big|_{\mathbf{u}_{ss}} \omega_1 - \left[Da_1 \exp\left(\frac{\gamma_1 \theta}{1 + \theta}\right) (1 - x) + \frac{\partial \mathcal{R}}{\partial y_B} \right] \Big|_{\mathbf{u}_{ss}} \omega_2 - \\ & Da_1 \exp\left(\frac{\gamma_1 \theta}{1 + \theta}\right) (1 - y_A - y_B) \Big|_{\mathbf{u}_{ss}} \omega_3 + \\ & \left. \left(\frac{\partial \mathcal{G}_1}{\partial \theta} - \frac{\partial \mathcal{R}}{\partial \theta} \right) \Big|_{\mathbf{u}_{ss}} \omega_4 = \pm i\sigma_i \omega_1 \quad (17) \end{aligned}$$

$$\begin{aligned} & - \left(2Da_2 \exp\left(\frac{\gamma_2 \theta}{1 + \theta}\right) (1 - y_A - y_B) + \frac{\partial \mathcal{R}}{\partial y_A} \right) \Big|_{\mathbf{u}_{ss}} \omega_1 - \\ & \left(2Da_2 \exp\left(\frac{\gamma_2 \theta}{1 + \theta}\right) (1 - y_A - y_B) + 2Da_{-2} \exp\left(\frac{\gamma_{-2} \theta}{1 + \theta}\right) y_B + \right. \\ & \left. \frac{\partial \mathcal{R}}{\partial y_B} \right) \Big|_{\mathbf{u}_{ss}} \omega_2 + \left(\frac{\partial \mathcal{G}_2}{\partial \theta} - \frac{\partial \mathcal{R}}{\partial \theta} \right) \Big|_{\mathbf{u}_{ss}} \omega_4 = \pm i\sigma_i \omega_2 \quad (18) \end{aligned}$$

$$\begin{aligned} & \frac{1}{Pe_a^m} \frac{\partial^2 \omega_3}{\partial \eta^2} - \frac{\partial \omega_3}{\partial \eta} + \left(N_c \frac{\partial \mathcal{G}_1}{\partial x} \Big|_{\mathbf{u}_{ss}} - \frac{\mu_{mn}^2}{Pe_{e1}^m} \right) \omega_3 + N_c \frac{\partial \mathcal{G}_1}{\partial y_A} \Big|_{\mathbf{u}_{ss}} \omega_1 + \\ & N_c \frac{\partial \mathcal{G}_1}{\partial y_B} \Big|_{\mathbf{u}_{ss}} \omega_2 + N_c \frac{\partial \mathcal{G}_1}{\partial \theta} \Big|_{\mathbf{u}_{ss}} \omega_4 = \pm i\sigma_i \omega_3 \quad (19) \end{aligned}$$

$$\begin{aligned} & \frac{1}{Le} \left[\frac{1}{Pe_a^h} \frac{\partial^2 \omega_4}{\partial \eta^2} - \frac{\partial \omega_4}{\partial \eta} + \left(\beta N_c \frac{\partial \mathcal{R}}{\partial \theta} \Big|_{\mathbf{u}_{ss}} - \frac{\mu_{mn}^2}{Pe_{e1}^h} \right) \omega_4 + \right. \\ & \left. \beta N_c \frac{\partial \mathcal{R}}{\partial y_A} \Big|_{\mathbf{u}_{ss}} \omega_1 + \beta N_c \frac{\partial \mathcal{R}}{\partial y_B} \Big|_{\mathbf{u}_{ss}} \omega_2 \right] = \pm i\sigma_i \omega_4 \quad (20) \end{aligned}$$

$$\frac{1}{Pe_a^m} \frac{\partial \omega_3}{\partial \eta} = \omega_3 \quad \frac{1}{Pe_a^h} \frac{\partial \omega_4}{\partial \eta} = \omega_4 \quad \eta = 0 \quad (21)$$

$$\frac{\partial \omega_3}{\partial \eta} = \frac{\partial \omega_4}{\partial \eta} = 0 \quad \eta = 1 \quad (22)$$

where $\boldsymbol{\omega}(\eta) = (\omega_1, \omega_2, \omega_3, \omega_4)$ and σ is the complex eigenvalue at the Hopf bifurcation. σ_i and $2\pi/\sigma_i$ provide an estimate of the frequency and time period of the oscillations next to the bifurcation point. An oscillatory neutral stability point is found by a simultaneous solution of the 1-D transversally uniform steady-state problem (eqs 3, 4, 9, and 10 in which the transversal Laplacian operator is deleted) and this eigenvalue problem (eqs 17–22).

A 1-D base steady state ($\mathbf{u}_{ss}(\eta)$) in an adiabatic reactor is transversally uniform due to the no-flux boundary conditions. At very large values of R/d_p , the transversal Pe is very large, and therefore, the transversal terms (μ_{mn}^2/Pe_{e1}^m and μ_{mn}^2/Pe_{e1}^h) in eqs 19 and 20 become negligible. Thus, near the Hopf bifurcation point at a very large R/d_p , the bifurcation parameter Da at which eqs 17–22 are satisfied approaches that of the Hopf bifurcation of a transversally uniform 1-D state. To construct the neutral stability curve, we initially determine one steady state (near the Hopf bifurcation point) that becomes unstable to transversal disturbance at very large R/d_p . We then use pseudoarc length continuation of the simultaneous solution of eqs 3, 4, 9, and 10 and eqs 17–20 to construct the neutral stability curve, which bounds the parameter region in which

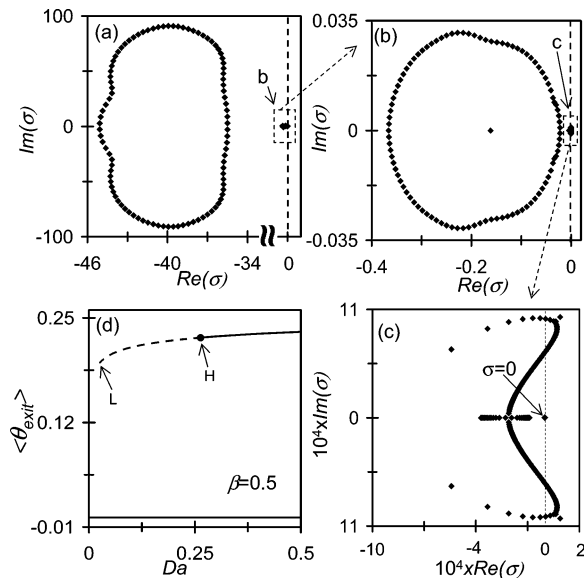


Figure 1. (a) The eigen spectrum at the limit point in the planes of $Im(\sigma)$ versus $Re(\sigma)$. (b) and (c) are the corresponding zoomed versions of the sections of the eigen spectrum in (a) and (b). (d) Bifurcation diagram of the transversally uniform state in the planes of $\langle\theta_{exit}\rangle$ versus Da . H = Hopf bifurcation, L = limit point, solid lines = stable, and dashed line = unstable.

the transversally uniform state is unstable to transversally inhomogeneous perturbations.

All the numerical simulations were conducted using the activation energies suggested by Slinko et al.²⁹ for the adsorption-desorption steps. The adsorption-desorption Da values are those used by Ivanov et al.²⁷ The kinetic and other parameters used in all the simulations were

$$\begin{aligned} \gamma_1 = 0, \quad \gamma_{-1} = 10.4, \quad \gamma_2 = 1.02, \quad \gamma_{-2} = 24.7, \\ Da_1 = 4.5 \times 10^{-4}, \quad L/d_p = 100 \\ Da_{-1} = 1.56 \times 10^{-5}, \quad Da_2 = 7.29 \times 10^{-4}, \\ Da_{-2} = 4.25 \times 10^{-7}, \quad \mu = 15 \quad (23) \end{aligned}$$

$$\begin{aligned} Le = 1000, \quad N_c = 4000, \quad \gamma_3 = 10.3, \quad Pe_a^m = 5.0L/d_p, \\ Pe_a^h = 1.0L/d_p \end{aligned}$$

We used an axial heat dispersion of heat that was 5 times larger than that of the mass, that is,

$$\frac{Pe_a^m}{Pe_a^h} = \frac{\bar{\lambda}_a/(\rho C_p)_g}{D_a} = 5.0 \quad (24)$$

The bifurcation diagram of the 1-D base states is shown in Figure 1d. The states on the middle unstable and the stable ignited branches are so close that they cannot be distinguished in the figure. A supercritical Hopf bifurcation exists on the ignited branch (point H in Figure 1a) at $Da = 0.293$. At the Hopf bifurcation point $\sigma_i = 0.001561$, which corresponds to an oscillation period ($2\pi/\sigma_i$) of 4025 next to the bifurcation point. Figure 1a shows the clusters formed by the first 400 eigenvalues close to the limit point L. Parts b and c of Figure 1 are the zoomed versions of the sections of parts a and b of Figure 1, respectively. The eigenvalues spectrum consists of three clusters (around $Re(\sigma) = -40$ in Figure 1a, around -0.2 in Figure 1b, and around 0 in Figure 1c), indicating that the dynamics of this system are affected by the interplay between three different characteristic time scales. At the limit point—where a real

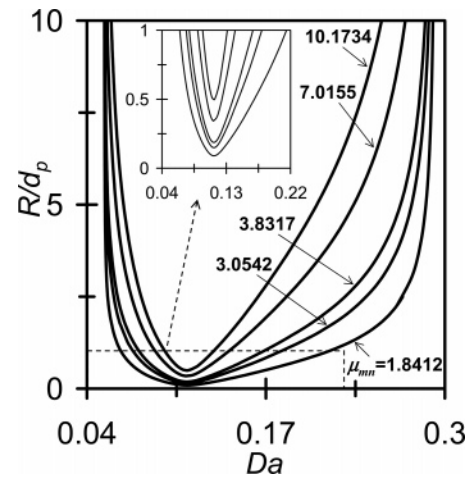


Figure 2. Oscillatory neutral stability curves for the first 3, 9th, and 15th transversal eigenmodes in the planes of R/d_p versus Da . (Note: 3rd, 9th, and 15th are the first three purely radial (no azimuthal dependence) modes.) Inset: Zoomed version of a segment of the oscillatory neutral stability curves.

eigenvalue crosses the imaginary axis—a cluster of complex eigenvalues with positive real parts exists (Figure 1c).

The i th mode is defined to be the one with the i th smallest transversal eigenmode number, μ_{mn} (solutions of eq 16). Figure 2 shows the neutral stability curves for the first 3 transversal modes, the 9th, and the 15th. The 3rd ($m = 0, n = 1, \mu_{mn} = 3.8317$), 9th ($m = 0, n = 2, \mu_{mn} = 7.0155$), and 15th ($m = 0, n = 3, \mu_{mn} = 10.1734$) are the first three purely radial (no azimuthal dependence) modes. The inset shows the distinct nature of the curves for small R/d_p . The right-hand asymptote of the neutral stability curves is at the Hopf bifurcation of the transversally uniform state ($Da = 0.293$ in Figure 2). However, no Hopf bifurcation of the transversally uniform state exists near the left asymptote. Each neutral stability curve is nested in the $(Da, R/d_p)$ plane within the one with a smaller μ_{mn} . This implies that different types of transversal hot zones may exist for the same Da . The number of these states increases for larger R/d_p .

Spatiotemporal Patterns

Numerical simulations of spatiotemporal patterns of the full 3-D reactor require extensive computer time and effort and are difficult to present in a paper. Thus, as a first step, we conducted and report here simulations of 2-D model, which can generate the azimuthally symmetric transversal hot regions in the (η, ξ) plane. These simulations were conducted by using finite differences in the axial and radial directions. We used 102 grid points in the axial direction and between 50 and 100 grid points in the radial direction. To circumvent the singularity at the center ($\xi = 0$), the grid points were placed at the radial positions $\xi_j = (2j - 1)/(2N - 1), \forall j = 1, N$.³¹ The dynamic simulations were conducted using a linear implicit extrapolator (LIMEX).^{32,33} The 1-D calculations were conducted using the LAPACK option. The 2-D calculations were conducted using a sparse iterative linear solver (GMRES/BiCGSTAB) that usually converged in 1–3 iterations. This discretized model is similar to a coupled-cell network, wherein the cells are placed in an equally spaced network of two dimensions. The cells communicate unequally with their nearest axial neighbors because the convection is unidirectional transport whereas the dispersion is bidirectional.

A transversal pattern is obtained only when the initial conditions are within the domain of attraction of that state. The set of initial conditions leading to the transversal nonuniform

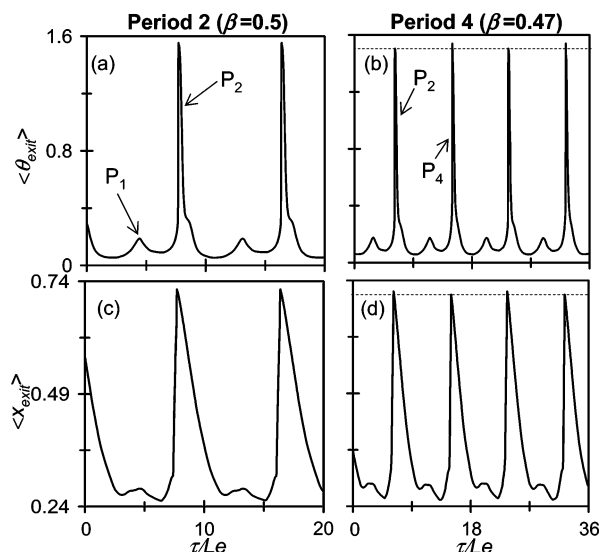


Figure 3. (a), (b) Average exit temperature, $\langle \theta_{\text{exit}} \rangle$, time series for period-2 and period-4 motions. (c), (d) Average exit conversion, $\langle x_{\text{exit}} \rangle$, time series for period-2 and period-4 motions.

states was selected in a procedure similar to that prescribed by Viswanathan and Luss.²³ To attain a spatiotemporal state corresponding to modes m and n , we start by selecting a set of R/d_p at a Da value slightly inside the corresponding (cup-shaped) neutral stability curve. We use as initial conditions

$$\mathbf{u}(\eta, \xi) = \mathbf{u}_{\text{ss}}(\eta) + A\omega_r(\eta)J_m(\mu_{mn}\xi) \quad (25)$$

where \mathbf{u}_{ss} are the state variables of the unstable 1-D state at the neutral stability point, ω_r is the real part of the eigenvectors of the eigenvalue problem in eqs 17–22, and A is a scalar coefficient that scales the perturbations and was typically chosen to be unity. When the state corresponding to the initial conditions (eq 25) did not evolve into a spatiotemporal state, the perturbations to the base (unstable) state \mathbf{u}_{ss} were scaled with another value of A in [0.01, 1.0]. After an initial transient, the simulation usually converged to a sustained spatiotemporal motion. We then used a sequence of dynamic simulations for slightly perturbed parameters to predict spatiotemporal states at the desired set of $(Da, R/d_p)$. As initial conditions corresponding to different transversal modes can lead to different spatiotemporal motions, we restricted our simulations to those evolving by use of the first azimuthally symmetric mode in eq 25.

Extensive numerical simulations were performed using this procedure for the transversal parameters

$$R/d_p = 30, \quad Pe_{\perp}^m = 30 \frac{(R/d_p)^2}{L/d_p}, \quad Pe_{\perp}^h = 10 \frac{(R/d_p)^2}{L/d_p} \quad (26)$$

(Note that the transversal dispersion of the heat is 3 times larger than that of the mass.) We present here simulations obtained at various β values and $Da = 0.214$. The initial conditions corresponded to the third transversal mode, which is the first azimuthally symmetric mode.

A slow change of the bifurcation variable β generated a cascade of complex periodic motions (period-2, -4, -8), which eventually led to formation of a spatiotemporal chaos. The time series of the average exit temperature and exit conversion of the period-2 motions (obtained for $\beta = 0.50$) are shown in parts a and c of Figure 3, respectively. (Note that the dimensionless time is scaled with respect to Le .) The first and the second rows in part I of Figure 4 consist of 2-D snapshots of the spatiotem-

poral temperature and conversion patterns obtained during the period-2 oscillations. The first three and the last four snapshots correspond to the smaller (P_1 in Figure 3a) and the larger (P_2 in Figure 3a) peaks in the time series of the period-2 motion, respectively. The dominant features of this motion are similar to those of the third transversal mode predicted by the linear stability analysis ($m = 0, n = 1$), which is the first azimuthally symmetric mode with the smallest value of $\mu_{mn} = 3.8317$. Several higher modes exert a small influence on the spatiotemporal motion. While the impact of the higher modes are suppressed in the temperature domain, their features are noticed in the snapshots of the conversion (Figure 4, part I–m). In all the period-2 motions that we simulated, the features corresponding to the higher (nondominant) modes always exit the reactor before the lower dominant ones, as can be observed from Figure 4, part I–m. The phase plane of the average exit conversion versus the average exit temperature of the period-2 oscillation, which consists of two loops, is shown in Figure 7a. The wiggles in one of the loops are caused by the variations in the average exit conversion because of the early exit of the features corresponding to the nondominant higher modes. (These wiggles are not noticeable in the average exit temperature and conversion time series as they occur during a very short time span.)

A decrease of β caused a shift from a period-2 to a period-4 motion. The time series of the average exit temperature and exit conversion of the period-4 (obtained for $\beta = 0.47$) motions are shown in parts b and d of Figure 3, respectively. The corresponding phase plane of the average exit conversion versus the average exit temperature, which consists of four loops, is shown in Figure 7b. Snapshots of corresponding spatiotemporal temperature patterns are shown in part II of Figure 4. The snapshots in the first row and the second row are taken during the first and the second half of the period-4 motion. In each half, a small peak and a large (temperature/conversion) peak exist. During the small peak, a hot zone emerges, moves downstream, and exits the reactor. During the large peak in the first half of the cycle, a hot zone emerges at the wall at some axial position—in this case at $\eta \approx 0.4$ —and then grows and captures the whole cross section of the reactor before rapidly moving downstream and exiting the reactor. The features of this hot zone are similar to those of the third mode, which is the first azimuthally symmetric mode. During the large peak in the second half of the cycle, one hot zone forms both at the wall and at the center (at $\tau/Le = 14.75$). This feature is similar to that of the ninth transversal mode ($m = 0, n = 2$), which is the second azimuthally symmetric mode with the second smallest value of μ_{mn} ($=7.0155$). These hot zones grow, merge, and then move downstream and exit the reactor. The periodic modulation of the third and ninth transversal modes may have been introduced by the period-doubling bifurcation to this period-4 spatiotemporal pattern. The time period of the first half and the second half of this motion are 8.5 and 9.5. Just as in the case of the period-2 oscillations, the nondominant modes contribute to the motion but are suppressed in the temperature domain. Once again, the wiggles in the phase plane (Figure 7b) are caused by the early exit of the motions generated by the higher modes.

As β was decreased from 0.47 to 0.465, the period-4 transformed to a period-8 motion. The time series of the exit temperature and the conversion time series are shown in parts a and c of Figure 5, while the corresponding phase plane is shown in Figure 7c. Representative snapshots of the corresponding spatiotemporal temperature patterns are presented in Figure 6 part I. The motion features switch from those similar

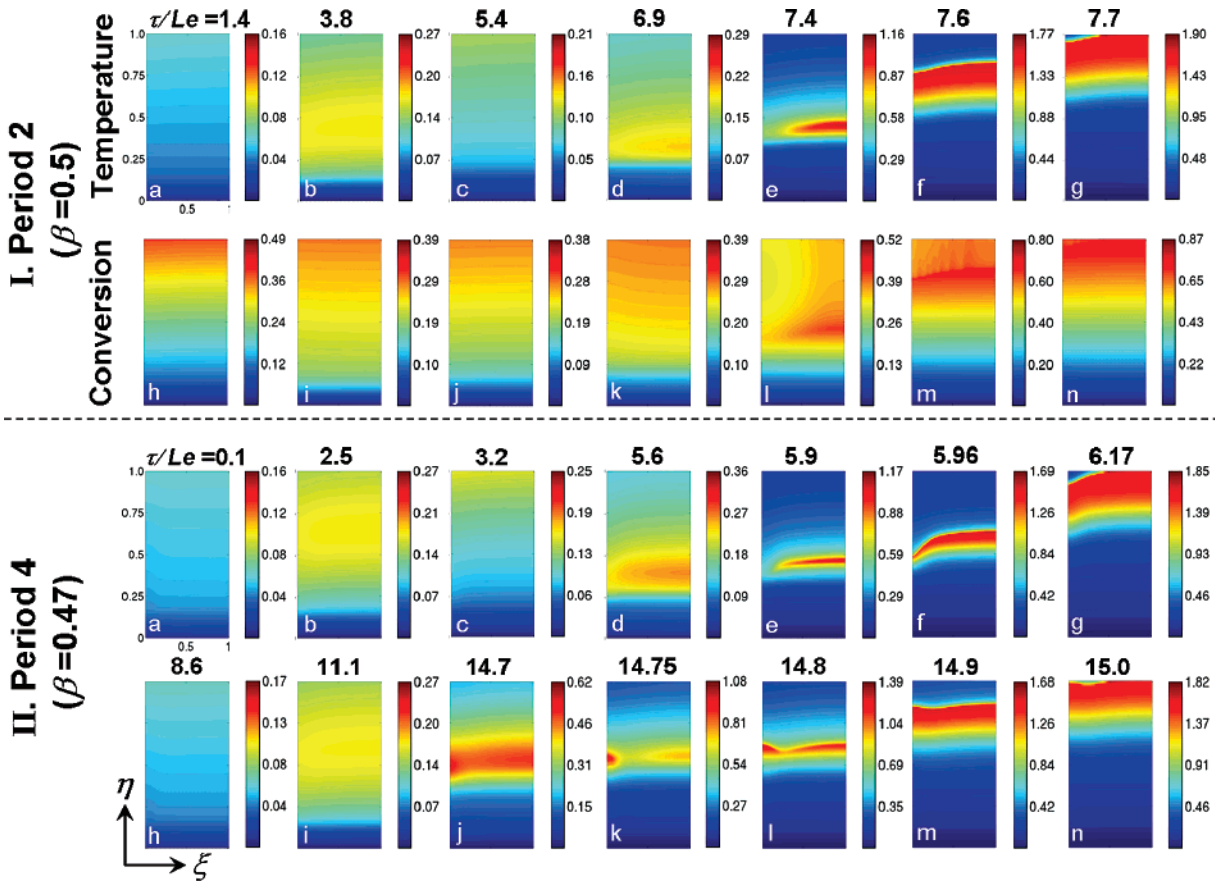


Figure 4. Part I, Row 1: Temperature contours of the reactor at various τ/Le during *period-2* motion. Part I, Row 2: Conversion contours of the reactor at various τ/Le during *period-2* motion. Part II: Temperature contours of the reactor at various τ/Le during *period-4* motion.

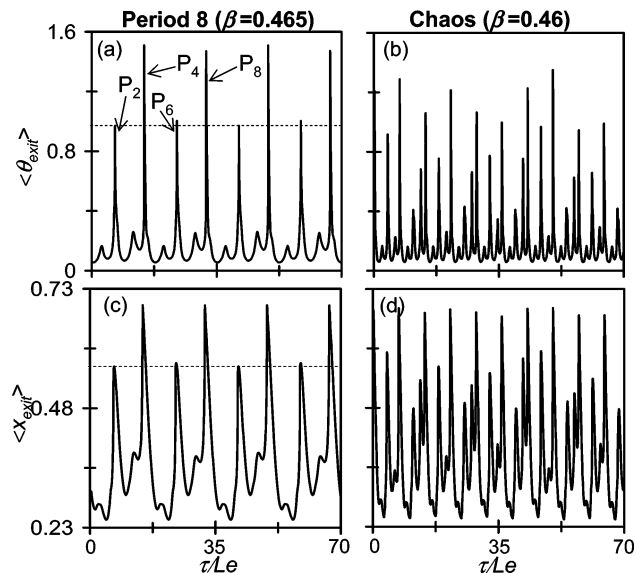


Figure 5. (a), (b) Average exit temperature, $\langle \theta_{exit} \rangle$, time series for period-8 motion and chaos. (c), (d) Average exit conversion, $\langle x_{exit} \rangle$, time series for period-8 motion and chaos.

to those of the third (Figure 6g) and to those of the ninth (Figure 6, part I–i to part I–k) transversal modes. Upon the bifurcation from period-4 to period-8, another temperature peak emerges between each pair of temperature peaks existing in the period-4 motion. This peak corresponds to a transversally uniform state, which, following its emergence, moves downstream and exits the reactor. A snapshot corresponding to this state is shown in Figure 6 part I for $\tau/Le = 6.0$.

As β is further decreased to 0.46, the spatiotemporal motion becomes chaotic. The corresponding time series of the exit tem-

perature and the conversion are shown in parts b and d of Figure 5. Figure 7d shows the phase plane of the chaotic motion. Snapshots of some of the temperature patterns generated during this spatiotemporal chaotic motion are shown in Figure 6 part II. Because of the rich structure of states that evolve in this case, we can show only some typical ones. The figure shows that the chaotic motion is caused by nonlinear interaction and modulation among various azimuthally symmetric modes and their coexistence. During the chaotic motion, one, two, or three hot zones form at some axial and radial locations, coalesce, move downstream, and exit the reactor. Next to every large peak in the time series, a small one exists, which sometimes corresponds to the motion of a transversally uniform state. This suggests that the chaotic motion may be due to shifts from one type of motion to another one.

An important feature that the simulations pointed out is that the measurable variables at the reactor exit do not provide any indication about the presence/absence of hot zones inside the reactor. This point can be readily discerned from Figure 8, which shows several projections of the phase plane for the period-2, period-4, and period-8 motions. Figure 8a shows the phase plane for the period-2 case of the instantaneous minimum versus maximum temperatures inside the reactor. Figure 8d shows the average exit temperature versus the instantaneous maximum conversion. Parts b and e and parts c and f of Figure 8 show similar phase plots for the period-4 and period-8 cases. As the hot zone moves downstream, the maximum temperature can exist at any one (or more) locations in the reactor. For example, in parts a and d of Figure 8, at point A, the average exit temperature ≈ 0.3 , whereas the maximum temperature ≈ 1.76 . A similar feature can be identified for the maximum local conversion. Parts c and f of Figure 8 illustrate

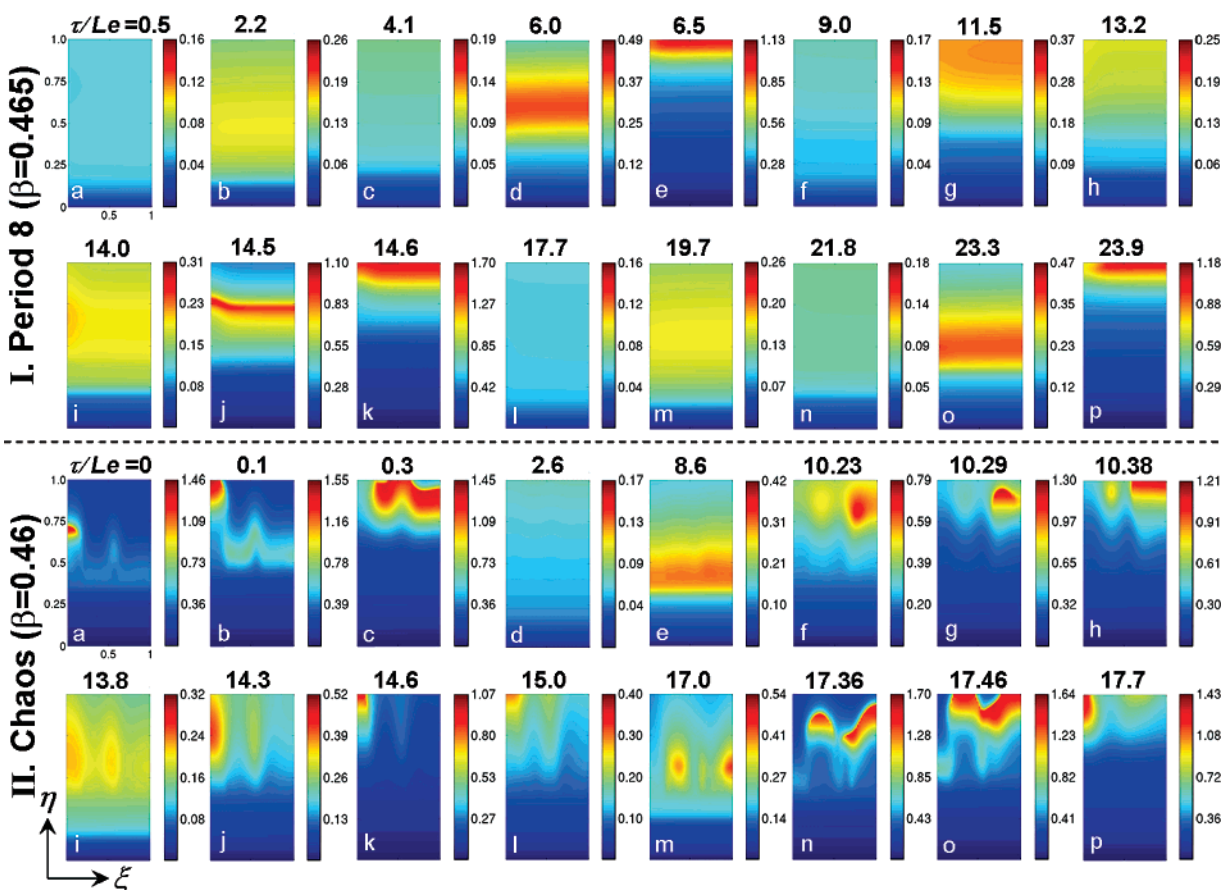


Figure 6. Part I: Temperature contours of the reactor at various τ/Le during *period-8* motion. Part II: Representative temperature contours of various spatiotemporal states in the reactor at various τ/Le during *chaos*.

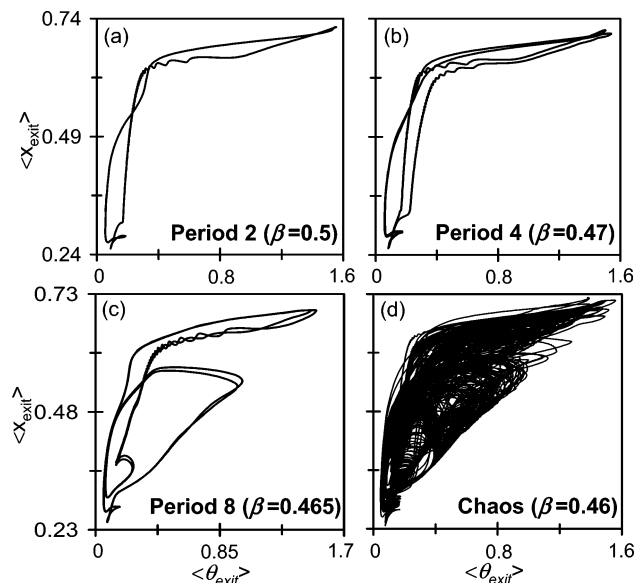


Figure 7. (a)–(d) are the phase plot in the planes of $\langle \theta_{exit} \rangle$ versus $\langle x_{exit} \rangle$ for period-2, period-4, and period-8 motions and chaos, respectively.

the same point for the period-8 motion. These two figures clearly show that a hot zone with a very high temperature may exist inside the reactor even when the spatial average exit temperature/conversion is low. Thus, measurements of the spatial average exit temperature/conversion may not enable detection of a hot zone with a very high temperature within the reactor.

Discussion and Conclusions

Until recently, mathematical models were not able to predict the observed transversal hot zones formation in uniformly

packed and active packed-bed reactors, while accounting for the fact the heat dispersion exceeds that of the reactants.²⁰ Neither can the simulations of transversal temperature patterns on the external surface of a thin catalytic cylindrical shell by Sheintuch's group^{12,17} predict the formation of hot zones in the cross section of an adiabatic packed-bed reactor, let alone their size and shape.

Viswanathan and Luss²³ showed that spatiotemporal patterns may be predicted to form in a shallow packed-bed reactor if the reaction can attain an oscillatory rate. This study shows that realistic reactor models may predict transversal hot zone formation also in long reactors used to conduct reactions having an oscillatory rate. Our analysis is based on the use of a pseudo-homogeneous model. The use of a two-phase model may lead to some quantitative changes but is not expected to change the fact that stable hot zones may exist for parameters bounded by the neutral stability curve. It is still an open question if and which other reaction mechanisms may predict this formation of transversal hot zones. Heat loss from the reactor walls and other kinetic reaction mechanisms (not necessarily oscillatory ones) are expected to generate other types of hot zones.

The numerical determination of the neutral stability curve is rather simple. The selection of initial conditions that are within the attraction domain of a stable state having transversal hot spots is more intricate, as a large fraction of the possible initial conditions will lead to a transversally uniform oscillatory state. Each neutral stability boundary is nested within that of a lower mode, that is, the one for $m = 0, n = N$ is nested within those for $m = 0, n = N - 1$. The numerical simulations of the 3-D model require extensive computer time and effort and are difficult to present in a paper. Thus, we restricted our dynamic simulations to the finding of transversal hot zones that are

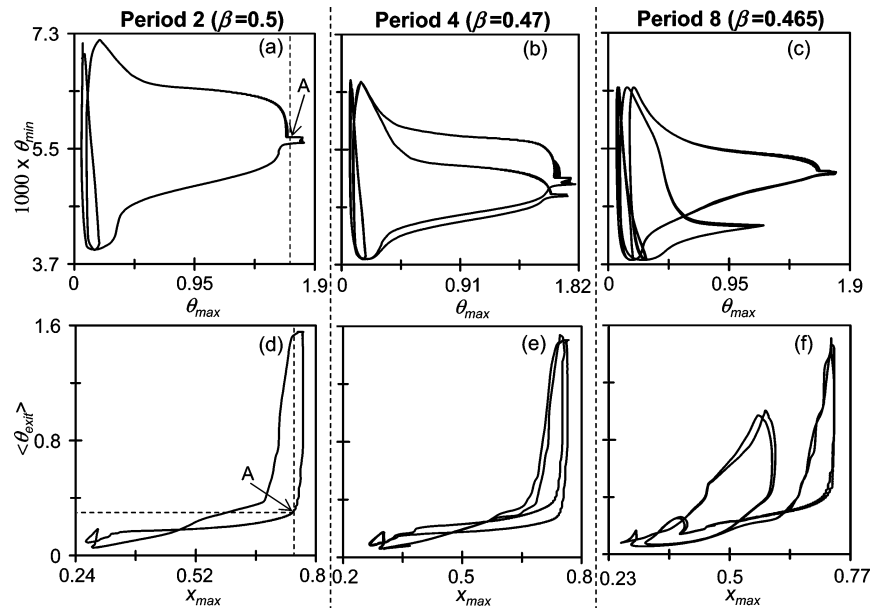


Figure 8. Phase plots for period-2 motion in the planes of (a) x_{\min} versus x_{\max} and (d) $\langle \theta_{\text{exit}} \rangle$ versus x_{\max} . Phase plots for period-4 motion in the planes of (b) θ_{\min} versus θ_{\max} and (e) $\langle \theta_{\text{exit}} \rangle$ versus x_{\max} . Phase plots for period-8 motion in the planes of (c) θ_{\min} versus θ_{\max} and (f) $\langle \theta_{\text{exit}} \rangle$ versus x_{\max} .

independent of the azimuthal position, that is, to rings of transversal hot regions. This simplification of the numerical efforts has obviously led to the finding of only a fraction of all the transversal hot zones that may exist in a long adiabatic packed-bed reactor. The simulations presented here are the first of the formation and dynamics of stable transversal hot zones in packed-bed reactors. It would be useful to conduct in the future the more complex and tedious simulations of the 3-D model, to determine if it exhibits, in addition to richer spatial patterns, also qualitatively different dynamic features.

Our simulations of the long adiabatic packed-bed reactor revealed some dynamic features that we did not find during the simulations of the shallow packed-bed reactor. The simulations of the long bed reactor revealed a period-2 bifurcation, that is, transitions among states having period- $2p$ features ($p = 1, 2, 3, \dots$). The simulations of the temporal motion revealed periodic modulation among the spatial features resembling different modes. For example, during about half of the time of the period-4 motion, the spatial features (Figure 4, part II-e, $\tau/Le = 5.9$) resembled those of the first mode ($m = 0, n = 1$), while during the remainder of the period (Figure 4, part II-k, $\tau/Le = 14.75$), they resembled those of the second azimuthally symmetric mode ($m = 0, n = 2$). During the period-8 motion, the spatial features resembled those of the first and second modes and the spatially uniform state. The finding that one of the modulated spatial features resembles those of a transversally uniform state is surprising, as one may expect that it will shift the reactor to the domain of attraction of the periodic stable, transversally uniform state. This did not happen, indicating that the motion was similar but not that of a stable periodic, uniform state.

Our simulations of the shallow adiabatic packed-bed reactor, in which the axial temperature and concentration gradients were neglected, did not reveal dynamic motions in which the spatial features during one period resemble those of different modes. This novel dynamic feature may be due to the fact that the dynamic features at each point in the reactor are affected by nonlinear interaction with the dynamic behavior in the upstream section. In a long reactor, the spatiotemporal transversal pattern at any axial position strongly affects the concentration and temperature fed to particles further downstream of that position.

This nonlinear coupling between the up- and downstream sections of the bed, which is not encountered in the shallow reactor model, is a possible explanation of this juxtaposition and modulation of the spatial features during the periodic spatiotemporal motions. This suggests that even more complex coupling and modulation is expected to be observed in the 3-D simulations.

The snapshots of the spatial temperature during the chaotic state (Figure 6-II) suggest that this state is generated by the nonlinear modulation and juxtaposition among motions corresponding to different modes. The simulation of the chaotic state (Figure 6-II) is the first to show formation of very small hot zones within a long bed. The “turbulent” formation and movement of the hot regions resembles the formation of turbulence in fluids because of the nonlinear interaction among motions corresponding to different modes.³⁴

Linear stability analysis indicates that a large number of modes exist in a reactor with a sufficiently large diameter. Thus, generation of chaos by a juxtaposition among trajectories corresponding to different modes is certainly a possibility. An important question is whether other complex motions exist and how to predict these. Use of a coupled-cell network model may enable tackling this question. A packed-bed reactor may be mimicked as a network of cells with each cell representing one catalyst particle and the surrounding fluid. The discretized model is similar to a coupled-cell network, wherein the cells are placed in an equally spaced network of 2 or 3 dimensions with *unequal* communication between the nearest neighbors. Stewart et al.³⁵ presented a comprehensive method to predict different structures that may form in various coupled-cell networks. Golubitsky et al.³⁶ presented several examples of those. Application of this method may provide useful insights on the structures that may exist and on how to predict them.

The presence of small local hot zones is very difficult to detect in large industrial reactors. The simulations shown in Figure 8 indicate that measurement of the effluent concentration and temperature may fail to detect the presence of hot zones in the reactor, especially small ones. Since the most dangerous situation occurs when the hot zones are located next to the reactor walls, one may attempt to detect these by use of infrared monitoring of the reactor walls or by painting the exterior reactor wall with a temperature sensitive paint. There exist at present no efficient

tools for measurement of small hot zones inside a large-scale reactor. Gladden's group³⁷ has attempted the use of magnetic resonance imaging (MRI) for noninvasive measurement of the local fluid properties at various positions in small packed-bed reactors. Gladden³⁸ suggested that local temperature may be measured using this technique. Development of this method may enable the detection of hot zones within laboratory reactors.

This study is the first step in the determination and understanding of local hot zones formation and motion inside a uniform, long packed-bed reactor. Richer and more dynamics are expected to be discovered by 3-D simulations. Even more complex features will be generated by accounting for local nonuniformities in the bed packing and/or activity. Heat loss from the reactors walls is expected to generate even more intricate dynamic features.

Acknowledgment

We thank the Welch Foundation, the ACS-PRF, the NSF, and the BSF for support of this research. Computations were performed at the Department of Mathematics, University of Houston, and the San Diego Supercomputing Center. We are most grateful to Prof. Martin Golubitsky, Dr. Andrew Salinger, and Dr. Grigorios Kolios for helpful discussions and advice.

Appendix I

Codimension-1 Locus: Hopf Neutral Stability Curves. A neutral stability point satisfies the codimension-1 problem

$$F(\mathbf{u}_{ss}(\eta), Da) = 0 \quad (\text{AI-1})$$

$$[D_{\mathbf{u}}F|_{\mathbf{u}_{ss}} - P](\boldsymbol{\omega}_r(\eta) \pm i\boldsymbol{\omega}_i(\eta)) = \pm i\sigma_i(\boldsymbol{\omega}_r(\eta) \pm i\boldsymbol{\omega}_i(\eta)) \quad (\text{AI-2})$$

where F is the steady-state 1-D model equations, and $D_{\mathbf{u}}F|_{\mathbf{u}_{ss}}$ is the first Fréchet derivative of F with respect to the state variables $\mathbf{u}(\eta)$ evaluated at the 1-D base steady-state $\mathbf{u}_{ss}(\eta)$. P is the transverse perturbation matrix, σ_i is the coefficient of the imaginary eigenvalue, and $\boldsymbol{\omega}(\eta) = \boldsymbol{\omega}_r(\eta) \pm i\boldsymbol{\omega}_i(\eta)$ are the corresponding complex eigenvectors. A neutral stability point is obtained by solving eq AI-1 simultaneously with

$$[D_{\mathbf{u}}F|_{\mathbf{u}_{ss}} - P]\boldsymbol{\omega}_r(\eta) + \sigma_i\boldsymbol{\omega}_i(\eta) = 0 \quad (\text{AI-3})$$

$$[D_{\mathbf{u}}F|_{\mathbf{u}_{ss}} - P]\boldsymbol{\omega}_i(\eta) - \sigma_i\boldsymbol{\omega}_r(\eta) = 0 \quad (\text{AI-4})$$

$$\|\boldsymbol{\omega}_r(\eta)\| + \|\boldsymbol{\omega}_i(\eta)\| - 1 = 0 \quad (\text{AI-5})$$

$$\boldsymbol{\omega}_r(\eta) \cdot \boldsymbol{\omega}_i(\eta) = 0 \quad (\text{AI-6})$$

A neutral stability curve is obtained by the pseudo-arc length continuation of a neutral stability point with respect to R/d_p .

Notations

a_v = catalyst specific surface area, $\text{m}_{\text{surf}}^2/\text{m}^3$
 A = constant coefficient for initial conditions in eq 23
 C = concentration, mol/m^3
 C_p = specific heat capacity, $\text{J kg}^{-1} \text{K}^{-1}$
 d_p = particle diameter, m
 D = species diffusion coefficient, m^2/s
 Da = Damköhler number, defined by eq 8
 $D_{\mathbf{u}}F$ = first Fréchet derivative
 E = activation energy, J/mol
 F = vector of steady-state equations
 G_1 = dimensionless rate of adsorption of species A, defined by eq 5

G_2 = dimensionless rate of adsorption of species B, defined by eq 6

J_m = Bessel function of first kind

k = adsorption or reaction constant

L = length of the reactor, m

Le = Lewis number, defined by eq 11

M = adsorption capacity, $\text{mol}/\text{m}_{\text{surf}}^2$

N = radial grid points

N_c = dimensionless adsorption capacity, defined by eq 11

P = transversal perturbation matrix

r = radial coordinate, m

R = radius of the reactor, m

\bar{R} = universal gas constant, $\text{J mol}^{-1} \text{K}^{-1}$

R = dimensionless reaction rate, defined by eq 7

t = time, s

T = temperature, K

\mathbf{u} = vector of state variables

v = superficial fluid velocity, m/s

x = conversion, defined by eq 8

y = fractional surface coverage

z = axial coordinate, m

Greek Letters

β = adiabatic temperature rise, defined by eq 11

γ = dimensionless activation energy, defined by eq 8

ϵ = bed voidage

η = dimensionless axial coordinate, defined by eq 11

θ = dimensionless temperature, defined by eq 8

$\bar{\lambda}$ = effective thermal conductivity, $\text{W m}^{-1} \text{K}^{-1}$

μ = surface coverage factor

μ_{mn} = transversal eigenmodes

ξ = dimensionless radial coordinate, defined by eq 11

ρ = density, kg/m^3

σ = complex eigenvalue

τ = dimensionless time, defined by eq 8

ϕ = azimuthal coordinate

$\boldsymbol{\omega}$ = eigenvector

$\boldsymbol{\omega}_{mn}$ = transversal perturbation vector, defined by eq 15

$-\Delta H$ = heat of reaction, J/mol

Others

∇^2 = Laplacian in polar coordinates

Superscripts

m = mass

h = heat

Subscripts

a = axial

A = species A

B = species B

g = gas phase

i = imaginary

in = inlet

m = azimuthal mode number

n = radial mode number

r = real

s = solid

ss = steady state

\perp = transversal

Literature Cited

(1) Borekov, G. K.; Matros, Y. S.; Klenov, O. P.; Logovkoi, V. I.; Lakhmostov, V. S. Local nonuniformities in a catalyst bed. *Dokl. Akad. Nauk SSSR* **1981**, 258, 1418.

- (2) Matros, Y. S. *Unsteady processes in catalytic reactors*; Elsevier: Amsterdam, The Netherlands, 1985.
- (3) Barkelew, C. H.; Gambhir, B. S. Stability of Trickle-Bed Reactors. *ACS Symp. Ser.* **1984**, 237, 61.
- (4) Jaffe, S. B. Hot spot simulation in commercial hydrogenation processes. *Ind. Eng. Chem. Process Des. Dev.* **1976**, 15, 410.
- (5) Wicke, E.; Onken, H. U. Periodicity and chaos in a catalytic packed bed reactor for CO oxidation. *Chem. Eng. Sci.* **1988**, 43, 2289.
- (6) Wicke, E.; Onken, H. U. Bifurcation, periodicity and chaos by thermal effects in heterogeneous catalysis. In *From Chemical to Biological Organization*; Markus, M., Muller, S. C., Nicolis, G., Eds.; Springer-Verlag: Berlin; New York, 1988; p 68.
- (7) Marwaha, B.; Luss, D. Hot zone formation in packed bed reactors. *Chem. Eng. Sci.* **2003**, 58, 733.
- (8) Marwaha, B.; Sundarram, S.; Luss, D. Dynamics of transversal hot zones in shallow packed bed reactors. *J. Phys. Chem. B* **2004**, 108, 14470.
- (9) Marwaha, B.; Annamalai, J.; Luss, D. Hot zone formation during carbon monoxide oxidation in a radial flow reactor. *Chem. Eng. Sci.* **2001**, 56, 89.
- (10) Marwaha, B.; Luss, D. Formation and dynamics of a hot zone in radial flow reactor. *AIChE J.* **2002**, 48, 617.
- (11) Digilov, R.; Nekhamkina, O.; Sheintuch, M. Thermal imaging of breathing patterns during CO oxidation on a Pd/Glass cloth. *AIChE J.* **2004**, 50, 163.
- (12) Digilov, R.; Nekhamkina, O.; Sheintuch, M. Catalytic spatiotemporal thermal patterns during CO oxidation on cylindrical surfaces: Experiments and simulations. *J. Chem. Phys.* **2006**, 124, 34709.
- (13) Sundarram, S.; Marwaha, B.; Luss, D. Global coupling induced temperature patterns on top of packed bed reactors. *Chem. Eng. Sci.* **2005**, 60, 6803.
- (14) Subramanian, S.; Balakotaiah, V. Analysis and classification of reaction driven stationary convective patterns in a porous medium. *Phys. Fluids* **1997**, 9, 1674.
- (15) Benneker, A. H.; Kronberg, A. E.; Westerterp, K. R. Influence of buoyancy forces on the flow of gases through packed beds at elevated pressures. *AIChE J.* **1998**, 44, 263.
- (16) Nekhamkina, O.; Digilov, R.; Sheintuch, M. Modeling of temporally complex breathing patterns during Pd-catalyzed CO oxidation. *J. Chem. Phys.* **2002**, 119, 2322.
- (17) Nekhamkina, O.; Sheintuch, M. Moving waves and spatiotemporal patterns due to weak thermal effects in modes of catalytic oxidation. *J. Chem. Phys.* **2005**, 122, 194701.
- (18) Schmitz, R. A.; Tsotsis, T. T. Spatially patterned states in systems of interacting catalyst particles. *Chem. Eng. Sci.* **1983**, 38, 1431.
- (19) Balakotaiah, V.; Christaforatou, E. L.; West, D. H. Transverse concentration and temperature non-uniformities in adiabatic packed bed catalytic reactors. *Chem. Eng. Sci.* **1999**, 54, 1725.
- (20) Yakhnin, V.; Menzinger, M. On transverse patterns in catalytic packed bed reactors. *Chem. Eng. Sci.* **2001**, 56, 2233.
- (21) Viswanathan, G.; Bindal, A.; Khinast, J.; Luss, D. Stationary transversal hot zones in adiabatic packed bed reactors. *AIChE J.* **2005**, 51, 3028.
- (22) Viswanathan, G. A.; Luss, D. Model prediction of hot spots formation in shallow adiabatic packed-bed reactors. *AIChE J.* **2006**, 52, 1533.
- (23) Viswanathan, G. A.; Luss, D. Moving transversal hot zones in adiabatic, shallow packed bed reactors. *AIChE J.* **2006**, 52, 705.
- (24) Asakura, K.; Lauterbach, J.; Rotermund, H. H.; Ertl, G. Spatiotemporal concentration patterns associated with the catalytic oxidation of CO on Au covered Pt(110) surfaces. *J. Chem. Phys.* **1995**, 102, 8175.
- (25) Belyaev, V. D.; Slinko, M. M.; Slinko, M. G. Self-oscillations in the catalytic rate of heterogeneous hydrogen oxidation on nickel and platinum. In *Proceedings of the Sixth International Congress on Catalysis*; Bond, G. C., Wells, P. B., Tompkins, F. C., Eds.; The Chemical Society: London, U.K., 1976; Vol. 2, p 758.
- (26) Slinko, M. G.; Slinko, M. M. Self-oscillations of heterogeneous catalytic reaction rates. *Catal. Rev. Sci. Eng.* **1978**, 17, 119.
- (27) Ivanov, E. A.; Chumakov, G. A.; Slinko, M. G.; Bruns, D. D.; Luss, D. Isothermal sustained oscillations due to the influence of adsorbed species of the catalytic reaction rate. *Chem. Eng. Sci.* **1980**, 35, 795.
- (28) Slinko, M. M.; Jaeger, N. I. *Oscillating heterogeneous catalytic systems. Studies in Surface Science and Catalysis*; Elsevier: Amsterdam, The Netherlands, 1994; Vol. 86.
- (29) Slinko, M. M.; Kurkina, E. S.; Liauw, M. A.; Jaeger, N. I. Mathematical modeling of complex oscillatory behavior during CO oxidation over Pd zeolite catalyst. *J. Chem. Phys.* **1999**, 111, 8105.
- (30) Golubitsky, M.; Stewart, I.; Knobloch, E. Target patterns and spirals in planar reaction-diffusion systems. *J. Nonlinear Sci.* **2000**, 10, 333.
- (31) Middy, U.; Luss, D. Impact of global interaction on pattern formation on a disk. *J. Chem. Phys.* **1995**, 102, 5029.
- (32) Deuffhard, P.; Hairer, E.; Zugck, J. One-step extrapolation methods for differential-algebraic systems. *J. Numer. Math.* **1987**, 51, 501.
- (33) Ehrig, R.; Nowak, U.; Oeverdieck, L.; Deuffhard, P. Advanced extrapolations methods for large scale differential algebraic problems. In *High Performance Scientific and Engineering Computing (Lecture Notes in Computational Science and Engineering)*; Bungartz, H.-J., Durst, F., Zenger, C., Eds.; Springer-Verlag: Munich, 1999; Vol. 8, p 233.
- (34) Hof, B.; van Doorne, C. W. H.; Westerweel, J.; Nieuwstadt, F. T. M.; Faisst, H.; Eckhardt, B.; Wedin, H.; Kerswell, R. R.; Waleffe, F. Experimental Observation of Nonlinear Traveling Waves in Turbulent Pipe Flow. *Science* **2004**, 305, 1594.
- (35) Stewart, I.; Golubitsky, M.; Pivato, M. Symmetry groupoids and patterns of synchrony in coupled cell networks. *SIAM J. Appl. Dynam. Sys.* **2003**, 2, 609.
- (36) Golubitsky, M.; Nicol, M.; Stewart, I. Some curious phenomena in coupled cell systems. *J. Nonlinear Sci.* **2004**, 14, 207.
- (37) Anadon, L. D.; Sederman, A. J.; Gladden, L. F. Mechanism of the trickle-to-pulse flow transition in fixed-bed reactors. *AIChE J.* **2006**, 52, 1522.
- (38) Gladden, L. F. Magnetic resonance: Ongoing and future role in chemical engineering research. *AIChE J.* **2003**, 49, 2.

Received for review March 27, 2006
 Revised manuscript received July 25, 2006
 Accepted August 16, 2006

IE0603823